Chiral Phonons and Giant Magneto-Optical Effect in $CrBr_3$ 2D Magnet

Tingting Yin[†], Kanchan Ajit Ulman[§], Sheng Liu[†], Andrés Granados del Águila[†], Yuqing Huang[†], Lifa Zhang[○], Marco Serra[‡], David Sedmidubsky[‡], Zdenek Sofer[‡], Su Ying Quek[§, ⊥, ǁ, ∇*], Qihua Xiong[±, », ⌜*]

[†]Division of Physics and Applied Physics, School of Physical and Mathematical Sciences, Nanyang Technological University, Singapore 637371, Singapore

[§]Centre for Advanced 2D Materials, National University of Singapore, 6 Science Drive 2, 117546, Singapore

[○]NNU-SULI Thermal Energy Research Center and Center for Quantum Transport and Thermal Energy Science, School of Physics and Technology, Nanjing Normal University, Nanjing, China

[‡]University of Chemistry and Technology Prague, Technicka 5, Prague 16628, Czech Republic

[⊥]Department of Physics, National University of Singapore, 2 Science Drive 3, 117542, Singapore

[ǁ]NUS Graduate School, Integrative Sciences and Engineering Programme, National University of Singapore, Singapore 117456

[∇]Department of Materials Science and Engineering, National University of Singapore, 9 Engineering Drive 1, Singapore 117575

[±]State Key Laboratory of Low-Dimensional Quantum Physics and Department of Physics, Tsinghua University, Beijing 100084, P.R. China.

[»]Beijing Academy of Quantum Information Sciences, Beijing 100193, P.R. China

[⌜]Beijing Innovation Center for Future Chips, Tsinghua University, Beijing 100084, P.R. China

*To whom correspondence should be addressed. E-mails: qihua_xiong@tsinghua.edu.cn and phyqsy@nus.edu.sg.

Phonons with chirality determine the optical helicity of inelastic light scattering processes due to their nonzero angular momentum. Here we show that two-dimensional (2D) magnetic $CrBr_3$ hosts chiral phonons at the Brillouin-zone center. These chiral phonons are linear combinations of the doubly-degenerate E_g phonons, and the phonon eigenmodes exhibit clockwise and counterclockwise rotational vibrations corresponding to angular momenta of $l = \pm 1$. Such E_g chiral phonons completely switch the polarization of incident circularly-polarized light. On the other hand, the non-degenerate non-chiral A_g phonons display a giant magneto-optical effect under an external out-of-plane magnetic field, rotating the plane of polarization of the scattered linearly-polarized light. The corresponding degree of polarization of the scattered light changes from 91% to -68% as the magnetic field strength increases from 0 to 5 T. In contrast, the chiral E_g modes display no field dependence. Our results lay a foundation for the study of phonon chirality and magneto-optical phenomena in 2D magnetic materials, as well as their related applications, such as the phonon Hall effect, topological photonics, and Raman lasing.

INTRODUCTION

Chiral phonons have nonzero (pseudo-) angular momenta (PAM) of $l = \pm 1$, and are typically associated with phonon modes that exhibit circular vibrations of atomic sublattices. Phonon chirality has been theoretically predicted and experimentally observed in two-dimensional (2D) nonmagnetic van der Waals materials, such as transition metal dichalcogenides (TMDCs).[1-3] Due to their non-zero angular momenta, chiral phonons can reverse the helicity of an incident photon involved in a Raman scattering process.[4, 5] Phonon chirality plays a key role in controlling topological state[6] and quantum state,[7] and results in large thermal Hall signals.[8]

It is known that an external magnetic field breaks the time-reversal symmetry in non-magnetic materials[9, 10], leading to magneto-optical Faraday and Kerr rotation effects.[11, 12] Giant magneto-optical Raman effects have also been observed in non-magnetic InSe[13] and MoS_2.[14] These effects arise from the magnetic-field-induced Lorentz force on the electrons, which results in a large magnetic-field dependence of the Raman intensity for out-of-plane vibrational modes.

The recent discovery of long-range magnetic order in chromium trihalide (CrX_3, X = I, Br, Cl) 2D magnetic materials[15-20] has generated tremendous interest in potential 2D magnet-based spintronic applications, including spin transistors[21-23] and tunneling magnetoresistance devices.[24-27] In particular, $CrBr_3$, a ferromagnetic (FM) insulator, has attracted a lot of attention. Van der Waals heterostructures like $CrBr_3$/TMDCs[28, 29] and $CrBr_3$/graphene[30] have been widely studied to explore the magnetic proximity effect for developing next-generation spintronic devices. However, much of the fundamental physics responsible for the novel functionalities in this material, including chirality of phonons, spin-phonon coupling, and the magneto-optical effect, remains unexplored. Compared to CrI_3, which exhibits a distinct crystal structure[31], a complex interlayer stacking[32, 33] and coexistence of magnetic orders[34] upon cooling, $CrBr_3$ is a more stable 2D ferromagnet.[26] Thus, $CrBr_3$ is an ideal candidate for exploring the intrinsic phonon dynamics and their interplay with external magnetic field.

Here, we report the direct observation of chiral phonons and a giant magneto-optical Raman effect in magnetic 2D $CrBr_3$ through systematic Raman scattering measurements. Our results show that the superposition of doubly degenerate E_g phonon modes results in chiral phonons with PAM of $l = \pm 1$. The phonon eigenmodes involve the circular motion of atoms, and these phonons completely switch the polarization of incident circularly-polarized light. On the other hand, for the non-degenerate non-chiral A_g phonon modes, the relative intensities of the co- and cross-linearly polarized components of the scattered light show a large variation with magnetic field strength when an external out-of-plane magnetic field is applied. The corresponding degree of polarization (DOP) of the scattered light changes from 91% to -68% as the magnetic field strength increases from 0 to 5 T. This observed rotation of the polarization of the scattered light demonstrates a giant magneto-optical effect for non-chiral A_g phonon modes in $CrBr_3$. These results lay a foundation for the study of phonon chirality and magneto-optical phenomena in 2D magnetic materials.

RESULTS AND DISCUSSION

Lattice Dynamics in $CrBr_3$

The atomic structure of bulk $CrBr_3$ is shown in Figure 1a. It is a layered structure with each layer consisting of a honeycomb sublattice of Cr^{3+} ions sandwiched between two Br atomic planes. Bulk $CrBr_3$ has a rhombohedral structure (space group C_{3i}^2 (S6)). The unit cell of this structure is highlighted by the dashed lines in Figure 1a and shows a FM ground state below the Curie temperature (T_c) with spins aligned out-of-plane (the green arrows). Phonon frequencies of few-layer 2D materials can depend on the number of layers and the stacking order, as previously observed in Raman spectra for TMDCs[35-38] and CrI_3.[39] However, our Raman results for $CrBr_3$ are independent of the number of layers, as shown in the thickness-dependent Raman spectra in Figure S1. In the rest of this paper, we focus on bulk $CrBr_3$, due to the larger Raman intensities in these samples.

In Figure 1b, we present our experimental Raman spectra for $CrBr_3$, measured in the FM phase at 10 K using linearly polarized light. Both co-polarization (XX) and cross-polarization (XY) geometries are used, with the first 'X' representing the polarization of the incident laser beam and the second 'X/Y' representing the polarization of the scattered light, selected using a polarizer. Four distinct Raman peaks are observed. Based on first principles density functional theory calculations for the zone-center phonon frequencies (see Table S1), it can be deduced that the two peaks at 106.6 and 184.5 cm^{-1} correspond to A_g modes and the two peaks at 143.3 and 153.1 cm^{-1} correspond to E_g modes. Our results are consistent with previously reported Raman results for bulk $CrBr_3$.[40] The inset to Figure 1b presents the theoretically simulated Raman spectra for bulk $CrBr_3$, which is in excellent agreement with our experimental data. It is important to notice that our linear-polarization Raman results exhibit distinct selection rules for A_g and E_g modes. For the A_g modes, the Raman signal vanishes in the XY configuration, *i.e.,* when the out-going light has a polarization axis perpendicular to that of the incoming light. On the other hand, the E_g modes do not show any dependence on the polarization direction of incident and scattered light. The dependence is clear

in the polar plot showing the angle-dependent Raman spectra in Figure 1c, where a circular shape indicates isotropic intensity for E_g phonon modes, in contrast to the angle-dependent Raman intensity for A_g phonon modes.

The top view of eigenvectors of these four modes is schematically shown in Figure 1d. The two A_g modes arise primarily from vibration of the Br atoms; the motion is mainly out-of-plane for A_g^2 (angle of 28.4 degrees with respect to the *z* axis) and in-plane for A_g^1 (angle of 61.7 degrees with respect to the *z* axis). The two E_g modes are degenerate, resembling an in-plane shearing motion of the Br atomic planes for E_g^2 and involving as well Cr atoms for E_g^1. However, small out-of-plane displacements are found for both E_g modes.

Phonon Chirality in $CrBr_3$

Chiral phonon modes originate from the circular vibration of sublattices, which can be probed by circularly polarized photons.[4, 5] Here, we perform helicity-resolved Raman scattering measurements at 10 K in the FM phase (Figure 2a) to resolve the chirality of E_g modes. The corresponding polar plot is presented in Figure 2b. We observe that Raman peaks corresponding to E_g modes appear only in the cross-circularly polarized configuration (σ^+ in σ^- out), which means that Raman scattering involving E_g modes reverses the helicity of the incident photons. In contrast, Raman scattering involving the two A_g modes does not change the helicity of the incident photons (Figure 2c). These results are in good agreement with the theoretical simulations shown in Figure S4.

Since $CrBr_3$ belongs to the magnetic double group of $S_6(-3)$, at Brillioun zone center, the pseudo-angular momentum (PAM) of phonon modes can be deduced from the action of the C_3 operator (rotation by $2\pi/3$ about the *z* axis) on the phonon wavefunction.[1] From the character table of $S_6(-3)$ (shown in Section S6), we obtain $C_3E_g(l/r) = e^{\pm i2\pi/3}E_g(l/r)$. The contrasting helicity-resolved Raman spectra for the A_g and E_g modes can be simply understood from the symmetry of the Raman tensor (Section S5). At the same time, conservation of PAM in the Raman process dictates that $l_s = l_i - l_{ph}$, where l_i, l_s and l_{ph} are respectively the angular momenta of the incident light, scattered light and the phonon involved in the Raman process,[1, 2], thus the process can be either $l_s(+1) = l_i(-1) - l_{ph}(+1)$ or $l_s(-1) = l_i(+1) - l_{ph}(-1)$. The PAM due to the photon can only be 1 or -1. Since Raman scattering involving E_g modes switches the polarization of circularly polarized light, the E_g modes in $CrBr_3$ must have a non-zero PAM. Single-phonon Raman scattering process can only include zone-center phonons due to the conservation of crystal momentum. However, the zone-center phonons have real eigenvectors which have zero phonon circular polarization by definition[1], as discussed in Section S7. Thus, the only zone-center Raman active phonon modes that can reverse the helicity of incoming light are a complex superposition of the degenerate E_g modes, as demonstrated by Figure 2d. In the Supplementary Information, we provide animated videos clearly showing the circular motion of the chiral phonon modes. The

phonon PAM of E_g modes are given by $l_{ph}[E_g(r)] = +1$ and $l_{ph}[E_g(l)] = -1$.[1, 2] Thus, the helicity-resolved Raman scattering results in Figure 2c can also be understood in terms of the chiral and non-chiral nature of the E_g and A_g modes, respectively.

We further calculate the magnitude of phonon circular polarization for the E_g modes, as defined by Zhang *et al.* :[1, 2]

$$S_{ph}^{z} = \hbar \sum_{\alpha=1}^{N} (|\epsilon_{R\alpha}|^2 - |\epsilon_{L\alpha}|^2),$$

where $\epsilon_{R\alpha} = \frac{1}{\sqrt{2}}(x_\alpha - iy_\alpha)$ and $\epsilon_{L\alpha} = \frac{1}{\sqrt{2}}(x_\alpha + iy_\alpha)$ are the right- and left-circularly polarized components of each phonon eigenvector for the α-th atom in $CrBr_3$. As shown in Section S7, we obtain a value of $S_{ph}^{z} = \pm 0.721\hbar$ for the circularly-polarized E_g^1 (143.3 cm^{-1}) modes and $\pm 0.916\hbar$ for the circularly-polarized E_g^2 (153.1 cm^{-1}) mode (Table S2). Non-zero values of circular polarization for E_g modes are a signature of chirality, while the deviation from unity is due to the out-of-plane contribution to the E_g modes.

Magnetism-Assisted Phonon Renormalization in $CrBr_3$

Given the existence of a 2D long-range FM order below T_c in $CrBr_3$, it is natural to explore the magnetic effect on phonon properties upon cooling.[41-44] Here, we have performed temperature-dependent Raman measurements and carefully fitted the spectra to extract the temperature dependence of the phonon energies and linewidths (Figure S2). We accurately determined these parameters by fitting the raw data of the E_g^1 and A_g^2 modes using Voigt functions, plotted as Figure 3a-d. A comparison with the anharmonic phonon-phonon scattering theory provides an insight into the phonon renormalization. The gray solid lines in Figure 3a-d indicate the theoretical phonon frequencies $\omega_{anh}(T)$ based on the standard anharmonic model.[5, 41] In the temperature range between 290 K and 50 K, a conventional hardening of phonons with decreasing temperature is observed due to the suppression of the anharmonic phonon-phonon interactions (Figure 3a and 3c). The temperature dependence becomes much stronger with the onset of magnetic ordering below 50 K, as demonstrated by the additional anomalous phonon hardening and the large deviation of phonon energies. Such a hardening of phonons is observed even at temperature above 50 K due to the short-range local ordering of magnetic moments. Similarly, the temperature dependence of the phonon linewidths also reveals a clear anomaly below 50 K, as demonstrated by Figure 3b and 3d. This anomalous behavior of linewidths below 50 K can be attributed to several factors including spin-phonon coupling, spin-induced negative thermal expansion[45] and magnetic ordering in the sample. We have performed the magnetic susceptibility measurement (Figure 3e) and fitted the χ^{-1} versus T plot (inset) by using Curie-Weiss law $\chi^{-1} = \frac{(T-\theta_{CW})}{C}$ to get the $\theta_{CW} = 47$ K, which is consistent with the FM interaction in $CrBr_3$ and agrees well with the predicated T_c point from our temperature-dependent Raman results. It has been suggested that phonon renormalization is proportional to the nearest-neighbor spin-spin correlation $<\vec{S_i}, \vec{S_j}>$,[43] and the spin-phonon

coupling coefficients can be extracted by using this equation: $\omega(T) \sim \omega_{anh}(T) + \lambda<\vec{S_i}, \vec{S_j}>$, where $\omega(T)$ is the measured phonon frequency, $\omega_{anh}(T)$ is the phonon frequency without spin-phonon coupling and λ represents the coupling strength. The shift in the frequency, $\omega(10K) - \omega_{anh}(70K)$, can be observed from Figure 3a and 3c. The measured saturated magnetization value of $CrBr_3$ is $3\mu_B$ per Cr atom (Figure 3f), consistent with a high spin configuration state of Cr^{3+}.[46] Therefore, the value of $<\vec{S_i}, \vec{S_j}>$ is 9/4 (S= 3/2) at 10 K,[47] and the coupling strength λ is calculated to be 0.51 and 0.31 cm^{-1} for E_g^1 and A_g^2 modes, respectively. The obtained coupling strength is large and comparable to previous observed value in other Cr-based ternary 2D magnets.[5, 48] In the Supplementary Information, we also demonstrate that the onset of magnetism in $CrBr_3$ below T_c will not induce structural transition (Figure S2) and the corresponding Raman selection rule remains the same in the paramagnetic (PM) phase at 290 K (Figure S3).

Magneto-Optical Effect in $CrBr_3$

We note that ferromagnetic order below T_c should result in an additional term in the Raman tensor that is imaginary and anti-symmetric in nature.[49, 50] This leads to off-diagonal components in the Raman tensor for the A_g modes which should result in a non-zero Raman intensity for the XY polarization configuration. However, the Raman intensities for the A_g modes in the XY polarization configuration have been essentially within the noise level, indicating that the off-diagonal terms in the Raman tensor are negligible. Since the magnitude of the antisymmetric Raman tensor induced by the magnetic field increases with the strength of the magnetic field[49] (see also Section S8), we explore the magneto-optical effects in $CrBr_3$ by performing magnetic-field-dependent Raman measurements at 8 K under an out-of-plane magnetic field up to 5 T.

Figure 4a shows that the relative Raman intensities in the XX and XY polarization configurations for the A_g^2 mode changes significantly with the magnitude of the applied magnetic field. Specifically, the A_g^2 mode Raman intensity in the XX polarization configuration decreases while that in the XY configuration increases as the field strength increases from 0 to 5 T. The degree of polarization (DOP) of the Raman-scattered light, defined as $\frac{I_{\parallel}-I_{\perp}}{I_{\parallel}+I_{\perp}}$, is plotted in Figure 4b as a function of the external magnetic field. The DOP for the A_g^2 mode of $CrBr_3$ can be tuned from 91% to -68% with sweeping magnetic field from 0 to 5 T. As a reference, the DOP corresponding to the Si TO mode at 520 cm^{-1} is also plotted. In contrast to the results for the A_g^2 mode of $CrBr_3$, the DOP for the Si TO mode only exhibits a small change of ~ 10% as the magnetic field is increased from 0 to 5 T. The E_g modes are found to be essentially magnetic-field-independent, displaying a near-zero DOP (Figure 4b).

In the presence of an external magnetic field, electrons in the sample experience a Lorentz force $\vec{F_L} \sim \vec{v} \times \vec{B}$. Together with the oscillating in-plane electric field from the incident light, this Lorentz force results in an antisymmetric term in the Raman tensor that is dependent on the magnitude of the magnetic field B (see Section S8). The components α_{xy} and α_{xx} of the

polarizability tensor are related by $|\alpha_{xy}/\alpha_{xx}| \propto \left|\frac{B}{B_0}\right|$, where $B_0 = \frac{m\gamma}{e}\left[1 - i\frac{(\omega_0^2-\omega^2)}{\gamma\omega}\right]$ is a resonant magnetic-field like term which depends on the electronic mass m, charge e, damping parameter γ and natural frequency of the electrons ω_0. Taking into account the symmetries of the Raman tensor for the A_g mode, we deduce the magnetic-field dependence of the Raman intensities to be $I_{xx}^{A_g} \propto a^2\left|\frac{B_0}{B_0^2+B^2}\right|^2$ and $I_{xy}^{A_g} \propto \beta^2\left|\frac{B}{B_0^2+B^2}\right|^2$, where a and β are parameters denoting the components of the field independent Raman tensor. Similarly, from the symmetries of the Raman tensor for degenerate E_g modes, it can be shown that the DOP for the E_g modes is independent of *B*.

CONCLUSION

In summary, we observe, for the first time, the chirality of E_g phonon modes in $CrBr_3$ 2D magnet by using linear polarization- and helicity-resolved Raman scattering spectroscopy. The doubly degenerate E_g modes reverse the helicity of incident photon due to their chiral nature with PAM of $l = \pm 1$. Moreover, the magnetism-induced spin-phonon coupling effect in $CrBr_3$ has been revealed by temperature-dependent Raman measurement. Upon applying an external out-of-plane magnetic field, the non-chiral A_g modes display a giant magneto-optical Raman effect, originating from the magnetic field induced off-diagonal term α_{xy} in the polarizability tensor. On the other hand, the chiral E_g modes do not show any field dependence. Our results provide a solid basis for understanding novel physical phenomena in 2D magnets and prove the importance of tuning the magnetic and lattice degrees of freedom for designing novel 2D magnet-based device applications.

EXPERIMENTAL SECTION

Sample preparation

$CrBr_3$ was synthesized by direct reaction of chromium (99.99%, Alfa Aesar) and bromine (99.9999%, Sigma Aldrich) in quartz glass ampoule. First, chromium and bromine corresponding to 12 g of $CrBr_3$ were placed in quartz ampoule (30 × 200 mm) and purged with argon. Bromine was used in 5 at.% excess. Ampoule was sealed under high vacuum ($1x10^{-3}$ Pa), while the charge in ampoule was cooled with liquid nitrogen. Firstly, the reaction mixture was heated on 750 ℃ for 24 hours to provide complete reaction of Cr and Br_2 while the second end of ampoule was kept at temperature below 200 ℃. Crystal growth by vapor transport was performed in two zone tube furnace. The growth zone was first cleaned by 25 hours application of reverse gradient 800 / 600 ℃ for growth zone and source zone, respectively. Crystal growth was performed at thermal gradient 750 / 650 ℃ for 5 days. Ampoule was opened in argon filled glovebox and crystals were handled strictly under inert atmosphere.

A few layers of $CrBr_3$ were obtained *via* mechanical exfoliating $CrBr_3$ crystal using polydimethysiloxane (PDMS) as a stamp in a nitrogen-filled glovebox. Monolayer $CrBr_3$ was identified by using the optical contrast. After that, $CrBr_3$ flake with 1 L, 10 L and ~ 100 L was picked up by a PDMS stamp and transferred onto SiO_2 / Si substrate for Raman measurements. The sample is very stable in high-vacuum and low-temperature environment during Raman measurements.

Magnetic susceptibility measurements

Magnetic measurements were performed on PPMS EverCool II system from Quantum Design (2 K / 9 T system) using VSM attachment. The measurement was performed in PE holder loaded in argon atmosphere glovebox.

Raman scattering measurements

Raman scattering measurements were performed in the backscattering geometry using a Horiba HR800 micro-Raman system equipped with a liquid nitrogen cooled charge-coupled device (CCD). A cryostat (Cryo Industry of America, USA) was used to provide a continuous temperature from 8 K to 300 K by liquid helium flow. The excitation laser was introduced using a 50× long working-distance focus lens, and Raman signals were collected through the same lens, dispersed with a 1800 g/mm grating. Solid-state lasers with wavelength of 532 nm were used to excite the sample. 532 nm RazorEdge ultrasteep long-pass edge filters were mounted in front of the CCD detector to filter out the excitation lines.

Magneto-Raman scattering measurements

The sample was mounted in an optical probe, which was immersed inside a cryostat filled with liquid helium and inserted in the **XEM-102** superconducting magnet. The magnetic field is in Faraday configuration with a maximum field strength of 5 T. The optical Raman measurements

were performed using a home-built confocal microscope system in the backscattering geometry. All measurements were carried out at 8 K. A solid-state laser (λ = 532 nm) was focused onto the sample along the out-of-plane direction by a 50× magnetic field compatible objective. The backscattered Raman signals were dispersed with a 1800 g/mm grating, and recorded by a nitrogen-cooled silicon-CCD.

Polarization-resolved measurements

A quarter-wave plate was combined with a linear polarizer to generate the linear- and circularly-polarized excitation light. Another half-wave plate or quarter-wave plate was used for resolving the scattered light. A linear polarizer was placed before the entrance slit of the spectrometer to ensure that any change in the Raman intensity was due to the intrinsic polarization of the scattering not due to the polarization response of the spectrometer grating.

Theoretical calculations

Non-collinear spin-polarized density functional theory calculations were performed using the plane-wave pseudopotential-based code implemented in the Quantum ESPRESSO package,[51] within the local-density approximation (LDA)[52] for the exchange-correlation function. The interactions between the ion core and the valence electronic wavefunctions were described using a fully-relativistic projector-augmented wave approach.[53] A kinetic energy cutoff of 50 Ry for the wavefunction and 500 Ry for the charge density was used along with an energy cutoff of 10^{-10} Ry for the self-consistent cycle and a $6 \times 6 \times 6$ Monkhorst-Pack grid of *k*-points, to obtain converged energies and forces.

The phonon calculations for the non-collinear spin system of $CrBr_3$ were performed using the finite displacements method as implemented in the PHONOPY code[54] to obtain the phonon frequencies and eigenvectors at the Γ-point. The change in forces due to a set of symmetry determined displacements of the atoms within the unit-cell of $CrBr_3$ with a small amplitude of 0.02 bohr was used to determine the force-constant matrices.

The Raman tensor which is the first derivative of the dielectric susceptibility with respect to the phonon displacement was obtained using the method proposed by Umari et al.,[55] by taking the derivative of the atomic forces with respect to the applied static electric field. We applied electric field of different amplitudes with the smallest amplitude of 5×10^{-5} Ry a.u. (1 Ry a.u. = 3.63609×10^{11} V/m), with non-uniform increments (-15, -10, -7, -5, -2, 2, 5, 7, 10, 15 times 5×10^{-5} Ry a.u.) along the X, Y, and X+Y direction to determine the in-plane Raman tensor of $CrBr_3$. A systematic convergence check of the Raman spectra with respect to the electric field steps was performed to ensure that any numerical errors were negligible. The Raman activity with both linear and circular polarization of the electric field was then obtained using the Raman tensors.

Supporting Information

Supporting Information is available from the Wiley Online Library or from the author.

Acknowledgements

Q.X. gratefully acknowledges National Natural Science Foundation of China (No. 12020101003) and start-up grant from Tsinghua University. T.Y. acknowledges the support from the Singapore National Research Foundation via Competitive Research Programme (NRF-CRP-21-2018-0007). S.Y.Q. and K.A.U. acknowledge support from the Singapore National Research Foundation, Prime Minister's Office, under its medium-sized centre program. Computations were performed on the NUS Graphene Research Centre cluster and National Supercomputing Centre Singapore (NSCC). K.A.U. acknowledges support from the Provost's Office and from the Ministry of Education in Singapore under grants MOE2016-T2-2-132 and MOE2017-T2-2-139. Z.S. was supported by project LTAUSA19034 from Ministry of Education Youth and Sports (MEYS).

Author contributions

T. Y. and Q. X. conceived the idea and designed the experiments. T. Y. performed the temperature and magnetic-field dependent Raman measurements. K. A. U. carried out the theoretical analysis and first-principles calculations under the supervision of S.Y.Q.. Z.S. and M.S. perform crystal growth and D.S. performed the magnetic measurement. T. Y., K. A. U., S.Y.Q. and Q.X. wrote the manuscript. T.Y. and K.A.U. contributed equally to this work.

Conflict of Interest

The authors declare no conflict of interest.

Keywords

chiral phonons, pseudoangular momentum, magneto-optical effect, $CrBr_3$ ferromagnet, spin-phonon coupling

REFERENCE

[1] L. Zhang, Q. Niu, *Phys. Rev. Lett.* **2015**, *115*, 115502.

[2] H. Chen, W. Zhang, Q. Niu, L. Zhang, *2D Mater.* **2018**, *6*, 012002.

[3] H. Zhu, J. Yi, M.-Y. Li, J. Xiao, L. Zhang, C.-W. Yang, R. A. Kaindl, L.-J. Li, Y. Wang, X. Zhang, *Science* **2018**, *359*, 579.

[4] S.-Y. Chen, C. Zheng, M. S. Fuhrer, J. Yan, *Nano Lett.* **2015**, *15*, 2526.

[5] L. Du, J. Tang, Y. Zhao, X. Li, R. Yang, X. Hu, X. Bai, X. Wang, K. Watanabe, T. Taniguchi, D. Shi, G. Yu, X. Bai, T. Hasan, G. Zhang, Z. Sun, *Adv. Funct. Mater.* **2019**, *29*, 1904734.

[6] G. Jotzu, M. Messer, R. Desbuquois, M. Lebrat, T. Uehlinger, D. Greif, T. Esslinger, *Nature* **2014**, *515*, 237.

[7] X. Chen, X. Lu, S. Dubey, Q. Yao, S. Liu, X. Wang, Q. Xiong, L. Zhang, A. Srivastava, *Nat. Phys.* **2019**, *15*, 221.

[8] G. Grissonnanche, S. Thériault, A. Gourgout, M. E. Boulanger, E. Lefrançois, A. Ataei, F. Laliberté, M. Dion, J. S. Zhou, S. Pyon, T. Takayama, H. Takagi, N. Doiron-Leyraud, L. Taillefer, *Nat. Phys.* **2020**, *16*, 1108.

[9] T. Lan, B. Ding, B. Liu, *Nano Select* **2020**, *1*, 298.

[10] X. Song, S. Xie, K. Kang, J. Park, V. Sih, *Nano Lett.* **2016**, *16*, 5010.

[11] B. Huang, J. Cenker, X. Zhang, E. L. Ray, T. Song, T. Taniguchi, K. Watanabe, M. A. McGuire, D. Xiao, X. Xu, *Nat. Nanotechnol.* **2020**, *15*, 212.

[12] L. F. McAven, H. J. Ross, K. Shinagawa, P. H. Butler, *J. Phys. B* **1999**, *32*, 563.

[13] W. Fu, X. Zhao, K. Wang, Z. Chen, K. Leng, D. Fu, P. Song, H. Wang, L. Deng, S. J. Pennycook, G. Zhang, B. Peng, K. P. Loh, *Nano Lett.* **2020**, *20*, 5330.

[14] J. Ji, A. Zhang, J. Fan, Y. Li, X. Wang, J. Zhang, E. W. Plummer, Q. Zhang, *Proc. Natl. Acad. Sci. U. S. A.* **2016**, *113*, 2349.

[15] C. Gong, L. Li, Z. Li, H. Ji, A. Stern, Y. Xia, T. Cao, W. Bao, C. Wang, Y. Wang, Z. Q. Qiu, R. J. Cava, S. G. Louie, J. Xia, X. Zhang, *Nature* **2017**, *546*, 265.

[16] H. H. Kim, B. Yang, S. Li, S. Jiang, C. Jin, Z. Tao, G. Nichols, F. Sfigakis, S. Zhong, C. Li, S. Tian, D. G. Cory, G.-X. Miao, J. Shan, K. F. Mak, H. Lei, K. Sun, L. Zhao, A. W. Tsen, *Proc. Natl. Acad. Sci. U. S. A.* **2019**, *116*, 11131.

[17] H. Li, S. Ruan, Y.-J. Zeng, *Adv. Mater.* **2019**, *31*, 1900065.

[18] B. Huang, G. Clark, E. Navarro-Moratalla, D. R. Klein, R. Cheng, K. L. Seyler, D. Zhong, E. Schmidgall, M. A. McGuire, D. H. Cobden, W. Yao, D. Xiao, P. Jarillo-Herrero, X. Xu, *Nature* **2017**, *546*, 270.

[19] M. Gibertini, M. Koperski, A. F. Morpurgo, K. S. Novoselov, *Nat. Nanotechnol.* **2019**, *14*, 408.

[20] K. S. Burch, D. Mandrus, J.-G. Park, *Nature* **2018**, *563*, 47.

[21] S. Jiang, L. Li, Z. Wang, K. F. Mak, J. Shan, *Nat. Nanotechnol.* **2018**, *13*, 549.

[22] B. Huang, G. Clark, D. R. Klein, D. MacNeill, E. Navarro-Moratalla, K. L. Seyler, N. Wilson, M. A. McGuire, D. H. Cobden, D. Xiao, W. Yao, P. Jarillo-Herrero, X. Xu, *Nat. Nanotechnol.* **2018**, *13*, 544.

[23] S. Jiang, J. Shan, K. F. Mak, *Nat. Mater.* **2018**, *17*, 406.

[24] T. Song, X. Cai, M. W.-Y. Tu, X. Zhang, B. Huang, N. P. Wilson, K. L. Seyler, L. Zhu, T. Taniguchi, K. Watanabe, M. A. McGuire, D. H. Cobden, D. Xiao, W. Yao, X. Xu, *Science* **2018**, *360*, 1214.

[25] D. Ghazaryan, M. T. Greenaway, Z. Wang, V. H. Guarochico-Moreira, I. J. Vera-Marun, J. Yin, Y. Liao, S. V. Morozov, O. Kristanovski, A. I. Lichtenstein, M. I. Katsnelson, F. Withers, A. Mishchenko, L. Eaves, A. K. Geim, K. S. Novoselov, A. Misra, *Nat. Electron.* **2018**, *1*, 344.

[26] M. Kim, P. Kumaravadivel, J. Birkbeck, W. Kuang, S. G. Xu, D. G. Hopkinson, J. Knolle, P. A. McClarty, A. I. Berdyugin, M. Ben Shalom, R. V. Gorbachev, S. J. Haigh, S. Liu, J. H. Edgar, K. S. Novoselov, I. V. Grigorieva, A. K. Geim, *Nat. Electron.* **2019**, *2*, 457.

[27] S. Jiang, L. Li, Z. Wang, J. Shan, K. F. Mak, *Nat. Electron.* **2019**, *2*, 159.

[28] L. Ciorciaro, M. Kroner, K. Watanabe, T. Taniguchi, A. Imamoglu, *Phys. Rev. Lett.* **2020**, *124*, 197401.
[29] T. P. Lyons, D. Gillard, A. Molina-Sánchez, A. Misra, F. Withers, P. S. Keatley, A. Kozikov, T. Taniguchi, K. Watanabe, K. S. Novoselov, J. Fernández-Rossier, A. I. Tartakovskii, *Nat. Commun.* **2020**, *11*, 6021.
[30] C. Tang, Z. Zhang, S. Lai, Q. Tan, W.-b. Gao, *Adv. Mater.* **2020**, *32*, 1908498.
[31] K. Guo, B. Deng, Z. Liu, C. Gao, Z. Shi, L. Bi, L. Zhang, H. Lu, P. Zhou, L. Zhang, Y. Cheng, B. Peng, *Sci. China Mater.* **2020**, *63*, 413.
[32] A. McCreary, T. T. Mai, F. G. Utermohlen, J. R. Simpson, K. F. Garrity, X. Feng, D. Shcherbakov, Y. Zhu, J. Hu, D. Weber, K. Watanabe, T. Taniguchi, J. E. Goldberger, Z. Mao, C. N. Lau, Y. Lu, N. Trivedi, R. Valdés Aguilar, A. R. Hight Walker, *Nat. Commun.* **2020**, *11*, 3879.
[33] W. Jin, Z. Ye, X. Luo, B. Yang, G. Ye, F. Yin, H. H. Kim, L. Rojas, S. Tian, Y. Fu, S. Yan, H. Lei, K. Sun, A. W. Tsen, R. He, L. Zhao, *Proc. Natl. Acad. Sci. U. S. A.* **2020**, *117*, 24664.
[34] B. Niu, T. Su, B. A. Francisco, S. Ghosh, F. Kargar, X. Huang, M. Lohmann, J. Li, Y. Xu, T. Taniguchi, K. Watanabe, D. Wu, A. Balandin, J. Shi, Y.-T. Cui, *Nano Lett.* **2020**, *20*, 553.
[35] N. Ubrig, Z. Wang, J. Teyssier, T. Taniguchi, K. Watanabe, E. Giannini, A. F. Morpurgo, M. Gibertini, *2D Mater.* **2019**, *7*, 015007.
[36] X. Lu, X. Luo, J. Zhang, S. Y. Quek, Q. Xiong, *Nano Res.* **2016**, *9*, 3559.
[37] X. Luo, Y. Zhao, J. Zhang, Q. Xiong, S. Y. Quek, *Phys. Rev. B* **2013**, *88*, 075320.
[38] Y. Zhao, X. Luo, H. Li, J. Zhang, P. T. Araujo, C. K. Gan, J. Wu, H. Zhang, S. Y. Quek, M. S. Dresselhaus, Q. Xiong, *Nano Lett.* **2013**, *13*, 1007.
[39] T. Song, Z. Fei, M. Yankowitz, Z. Lin, Q. Jiang, K. Hwangbo, Q. Zhang, B. Sun, T. Taniguchi, K. Watanabe, M. A. McGuire, D. Graf, T. Cao, J.-H. Chu, D. H. Cobden, C. R. Dean, D. Xiao, X. Xu, *Nat. Mater.* **2019**, *18*, 1298.
[40] V. M. Bermudez, *Solid State Commun.* **1976**, *19*, 693.
[41] M. A. Prosnikov, A. N. Smirnov, V. Y. Davydov, R. V. Pisarev, N. A. Lyubochko, S. N. Barilo, *Phys. Rev. B* **2018**, *98*, 104404.
[42] S. Krannich, Y. Sidis, D. Lamago, R. Heid, J. M. Mignot, H. v. Löhneysen, A. Ivanov, P. Steffens, T. Keller, L. Wang, E. Goering, F. Weber, *Nat. Commun.* **2015**, *6*, 8961.
[43] Y. Sharma, S. Sahoo, W. Perez, S. Mukherjee, R. Gupta, A. Garg, R. Chatterjee, R. S. Katiyar, *J. Appl. Phys.* **2014**, *115*, 183907.
[44] X. Wang, K. Du, Y. Y. Fredrik Liu, P. Hu, J. Zhang, Q. Zhang, M. H. S. Owen, X. Lu, C. K. Gan, P. Sengupta, C. Kloc, Q. Xiong, *2D Mater.* **2016**, *3*, 031009.
[45] D. P. Kozlenko, O. N. Lis, S. E. Kichanov, E. V. Lukin, N. M. Belozerova, B. N. Savenko, *npj Quantum Mater.* **2021**, *6*, 19.
[46] H. Ji, R. A. Stokes, L. D. Alegria, E. C. Blomberg, M. A. Tanatar, A. Reijnders, L. M. Schoop, T. Liang, R. Prozorov, K. S. Burch, N. P. Ong, J. R. Petta, R. J. Cava, *J. Appl. Phys.* **2013**, *114*, 114907.
[47] T. J. Williams, A. A. Aczel, M. D. Lumsden, S. E. Nagler, M. B. Stone, J. Q. Yan, D. Mandrus, *Phys. Rev. B* **2015**, *92*, 144404.
[48] L. D. Casto, A. J. Clune, M. O. Yokosuk, J. L. Musfeldt, T. J. Williams, H. L. Zhuang, M.-W. Lin, K. Xiao, R. G. Hennig, B. C. Sales, J.-Q. Yan, D. Mandrus, *APL Mater.* **2015**, *3*, 041515.
[49] E. Anastassakis, E. Burstein, A. A. Maradudin, R. Minnick, *J. Phys. Chem. Solids* **1972**, *33*, 519.
[50] Y. Zhang, X. Wu, B. Lyu, M. Wu, S. Zhao, J. Chen, M. Jia, C. Zhang, L. Wang, X. Wang, Y. Chen, J. Mei, T. Taniguchi, K. Watanabe, H. Yan, Q. Liu, L. Huang, Y. Zhao, M. Huang, *Nano Lett.* **2020**, *20*, 729.
[51] P. Giannozzi, S. Baroni, N. Bonini, M. Calandra, R. Car, C. Cavazzoni, D. Ceresoli, G. L. Chiarotti, M. Cococcioni, I. Dabo, A. Dal Corso, S. de Gironcoli, S. Fabris, G. Fratesi, R. Gebauer, U. Gerstmann, C. Gougoussis, A. Kokalj, M. Lazzeri, L. Martin-Samos, N. Marzari, F. Mauri, R. Mazzarello, S. Paolini,

A. Pasquarello, L. Paulatto, C. Sbraccia, S. Scandolo, G. Sclauzero, A. P. Seitsonen, A. Smogunov, P. Umari, R. M. Wentzcovitch, *J. Phys. Condens. Matter* **2009**, *21*, 395502.
[52] J. P. Perdew, Y. Wang, *Phys. Rev. B* **1992**, *45*, 13244.
[53] P. E. Blöchl, *Phys. Rev. B* **1994**, *50*, 17953.
[54] A. Togo, I. Tanaka, *Scr. Mater* **2015**, *108*, 1.
[55] P. Umari, A. Pasquarello, *Diam. Relat. Mater* **2005**, *14*, 1255.

Figures and Captions

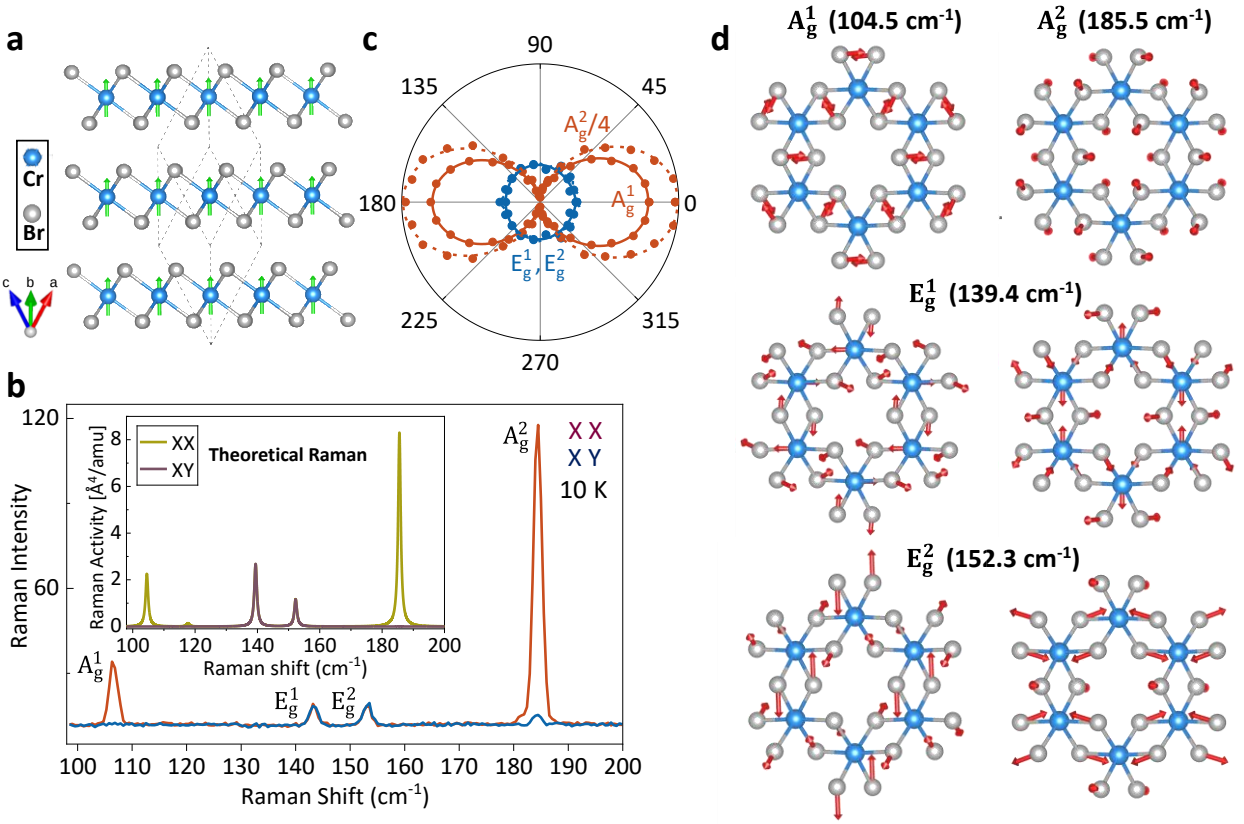

Figure 1. a) Side view of $CrBr_3$ in unit cell with rhombohedral structure, the spins aligned perpendicular to the basal plane in FM phase. b) Linear-polarization Raman spectra of bulk $CrBr_3$ in the co- polarization channel (XX, dark red) and cross-polarization channel (XY, dark blue) at 10 K under 532 nm excitation. The phonon modes are assigned and labeled as A_g^1, E_g^1, E_g^2 and A_g^2. Inset shows the corresponding simulated Raman spectra. c) Angle dependence of Raman intensity. d) Phonon eigenvectors with calculated frequencies of Raman-active modes at the Brillouin zone center in bulk $CrBr_3$.

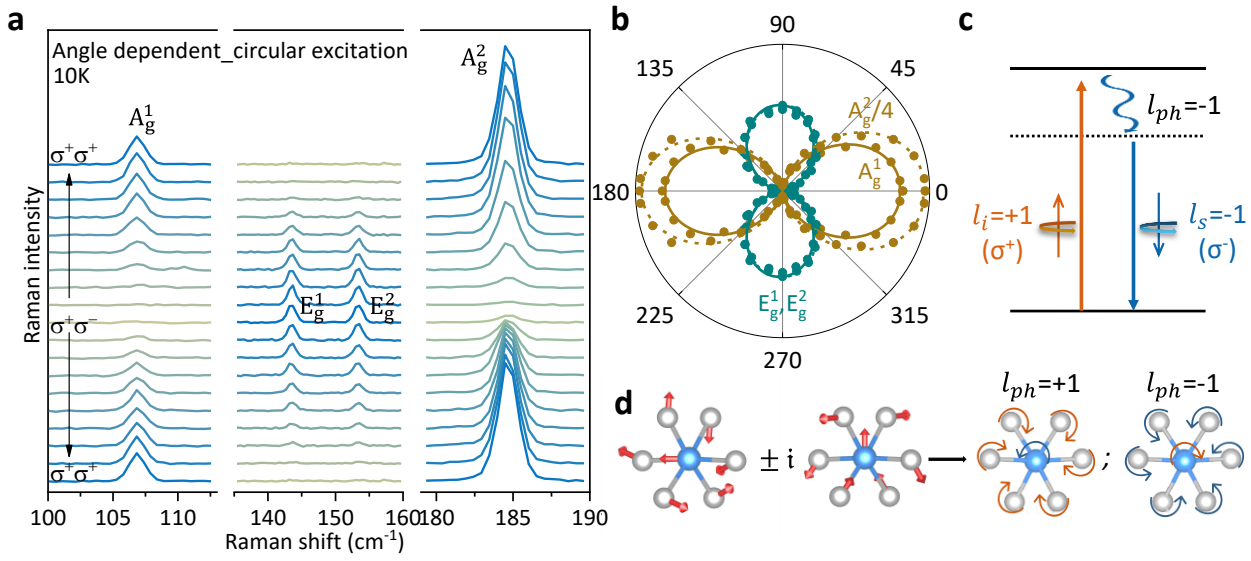

Figure 2. Chirality of Raman-active phonons of $CrBr_3$. a) Helicity-resolved Raman spectra of bulk $CrBr_3$ at 10 K. The excitation wavelength is 532 nm with σ^+ polarization. b) Polar plot of the Raman intensities of these four modes versus the rotation of the quarter-wave plate. The 0° and 90° correspond to the (σ^+, σ^+) and (σ^+, σ^-) configurations, respectively. c) Schematic of the helicity of photon switched by the chiral phonon. d) Superposition of two orthogonal linear vibrations of E_g^1 (143.0 cm^{-1}) results in right-handed or left-handed circular motions at the Γ-point, *i.e.*, chiral phonons with PAM of $l = \pm 1$.

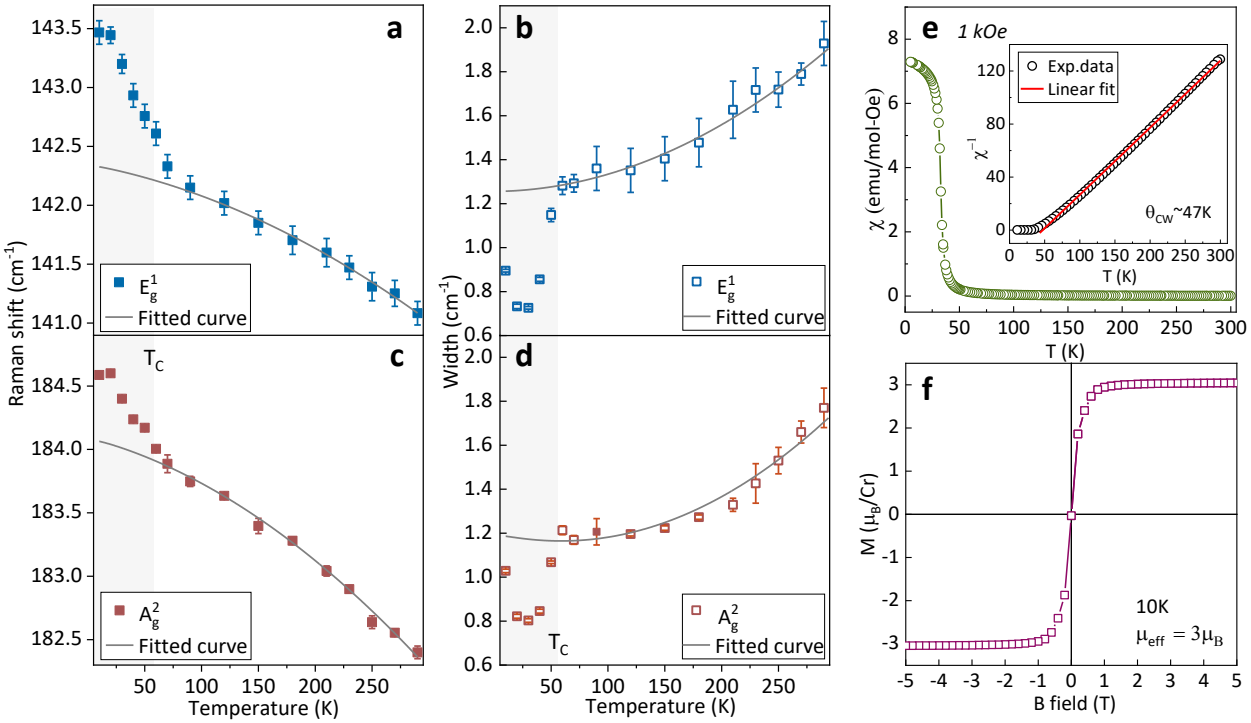

Figure 3. Spin-phonon coupling in $CrBr_3$. Evolution of phonon frequencies a, c) and phonon linewidths b, d) of E_g^1 and A_g^2 phonons with temperature decreasing from 290 K to 10 K. The gray solid lines indicate the fitting results by using the anharmonic model. FM phase below T_c is indicated by the shaded gray area. e) Magnetic susceptibilities of $CrBr_3$ bulk sample with 1 kOe field applied with decreasing temperature. Inset shows the plot of inverse susceptibility versus temperature and the red line shows a Curie-Weiss fitting, θ_{CW} = 47 K. f) Magnetic moment vs magnetic field at 10 K indicates that the saturated magnetic moment is $3\mu_B$ per Cr atom.

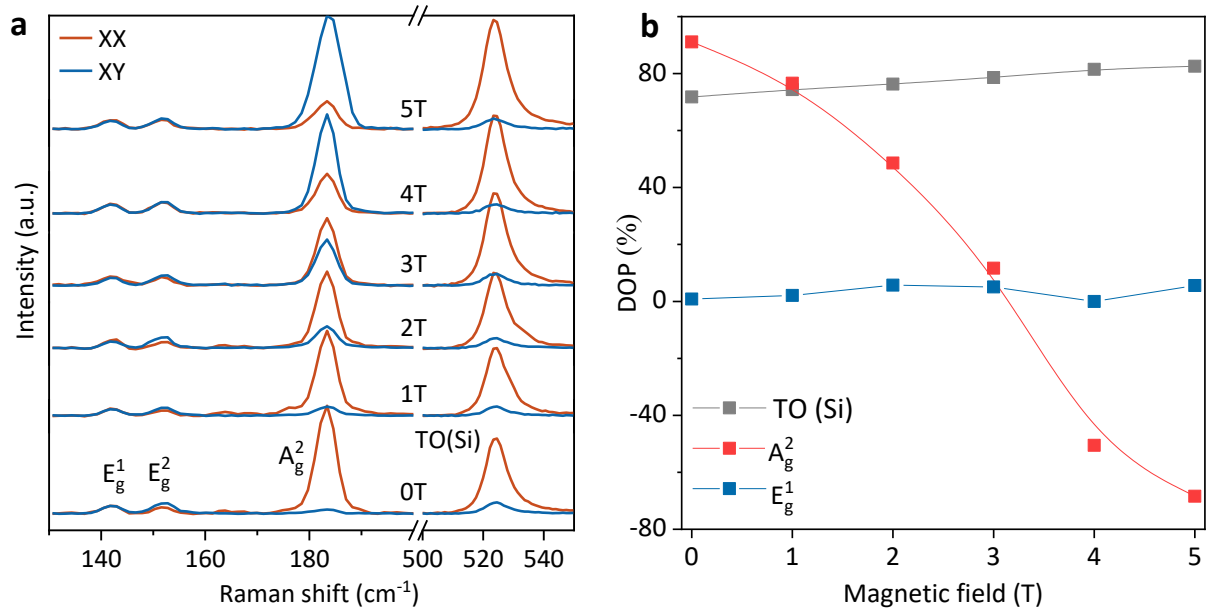

Figure 4. Magneto-optical Raman effect. a) Magnetic-field dependent Raman spectra of $CrBr_3$ in co- and cross-linearly polarized configurations at 8 K under 532 nm excitation (**B** ⊥ ***ab*** plane). b) Degree of polarization of A_g^2, E_g^1 phonons of $CrBr_3$ and TO phonon of Si as a function of magnetic field.